ORIGINAL RESEARCH Open access

Evaluation of UAV-Derived Multispectral and Surface Data for Object-Based Urban Land Cover Mapping

Ahmed El-Mansouri[1*], Fatima Zahra[2], Youssef Hariri[3]

Abstract

Advances in UAV sensor technology now allow multiple spectral image types to be captured during a single flight mission. This research used high-resolution images captured by UAVs over urban areas to generate detailed land-cover maps of categories such as roads, sidewalks, and street vegetation. Altogether, nine orthoimages were generated, and the key variables useful for creating UAV-based land cover maps were determined. From object-based image analysis, a total of 126 variables were obtained by calculating 14 statistical measures for every image. The random forest (RF) classifier served to rank the importance of these 126 variables. Following this, the RF model was optimized by reducing variables, and the value of high-priority variables was assessed by comparing the original and optimized RF models. Variable importance ranking identified the top factors in this sequence: normalized digital surface model (nDSM), normalized difference vegetation index (NDVI), land surface temperature (LST), soil adjusted vegetation index (SAVI), blue, green, red, rededge. Ultimately, multiple evaluations revealed no notable differences in classification outcomes between the initial and optimized RF models, despite using fewer variables.

Keywords Unmanned aerial vehicle, Random forest, OBIA, Variable importance, Land cover classification

*Correspondence:
Ahmed El-Mansouri
ahmed.elmansouri@uca.ma
[1] Department of AI for Argan Tree Health Monitoring and Nut Yield Forecasting, Faculty of Agriculture, University of Marrakech, Marrakech, Morocco
[2] Department of Machine Learning for Soil Moisture Prediction in Semi-Arid Regions, Faculty of Agriculture, University of Casablanca, Casablanca, Morocco
[3] Department of AI for Argan Tree and Cereal Crop Monitoring, Faculty of Agriculture, Mohammed V University, Rabat, Morocco

Introduction

Land cover maps are developed using defined classification frameworks that reflect the optical and physical properties of Earth's surface, serving as a core source of information for understanding regional conditions. In urban contexts, such maps provide essential scientific support for municipal planning tasks, including land suitability evaluation, environmental impact studies, and urban renewal projects. In scholarly work, they contribute significantly to investigations such as thermal environment studies, airflow modeling, and ecosystem monitoring [1-5]. In the Republic of Korea, nationwide land cover maps are updated every 1–10 years, depending on available government funding. Nevertheless, discrepancies in land cover representation can emerge because satellite and digital aerial images follow separate update schedules during map creation. Given that the smallest mapping unit in these nationwide efforts is fixed at surfaces exceeding 2500 m2, the maps lack sufficient detail for medium- and small-scale patches. For example, a small patch of grass beside a road is often categorized as road rather than vegetation because it does not meet the size requirement. Hence, producing land cover maps that deliver both high efficiency and precision for medium and small zones is crucial [6-9].

This is an open access article distributed under the terms of the Creative Commons Attribution-NonCommercial-ShareAlike 4.0 International License (CC BY-NC-SA 4.0), which permits non-commercial use, distribution, reproduction, and adaptation in any medium or format, provided that appropriate credit is given to the original author(s) and source, a link to the license is provided, and any changes made are indicated. Adapted material must be distributed under the same license.

© 2026 The Author(s). | Published by Agro Intelligence Research Press

Recent improvements in unmanned aerial vehicle (UAV) platforms and associated sensors have enhanced both spectral resolution and positional precision, leading to expanded adoption in aerial remote sensing applications [10-15]. The emergence of 4-band multispectral sensors, together with very high-resolution (VHR) RGB and thermal infrared sensors, enables the collection of diverse spectral datasets within a single mission. In addition, UAV imagery imposes minimal spatiotemporal constraints relative to satellite or traditional aerial photography, enabling greater adaptability for collecting data with superior spatiotemporal detail [16-18].

At present, investigators frequently rely on high-resolution UAV imagery to identify and study land cover categories in defined locations [19-22]. Yet, such high-resolution data display considerable spectral variation even for identical features [23-25]. Because individual objects require many pixels for representation, each pixel records structural and contextual differences. As a result, pixel-based classification of high-resolution UAV data often involves images with more than 10,000,000 pixels, increasing the risk of lower accuracy due to spectral inconsistencies.

Object-based image analysis (OBIA) has surfaced as an innovative strategy to address spectral variation, moving beyond conventional pixel-based techniques. Pixel-based methods handle pixels independently, whereas object-based methods combine neighboring pixels sharing similar traits to form and classify meaningful surface objects. This strategy minimizes spectral fluctuations arising from gaps, shadows, or surface textures. Moreover, it incorporates comprehensive details regarding geometry, texture, and context, which boosts classification performance when integrated with diverse vector and geospatial layers [26-29].

Numerous studies have used UAV-acquired datasets for OBIA-supported land cover mapping of compact and intermediate zones, combined with machine learning algorithms [20, 30-32]. Kilwenge *et al.* [33] deployed a fixed-wing UAV for multispectral (4 bands) capture and reached 95% accuracy across five classes—banana plantation, bare land, buildings, other vegetation, and water. Natesan *et al.* [34] equipped rotary-wing UAVs with RGB and NIR cameras to survey riverine zones (200 m × 100 m), securing 78% accuracy for four classes—grass, water, trees, and road. Lv *et al.* [35] employed UAV RGB imagery to test filtering techniques for distinguishing seven residential classes—buildings, grass, road, trees, water, soil, and shadows. Furthermore, Geipel *et al.* [36] assembled a UAV system using RGB sensors to forecast corn productivity. While UAV use in environmental domains continues to mature, its application to precise urban land-cover mapping and evaluation remains relatively scarce.

Intricate urban landscapes pose major obstacles to accurate classification, a phenomenon widely recognized as spectral confusion [37, 38]. Classification systems that rely exclusively on spectral properties struggle to address this challenge in cities [39]. Generating a broader range of features presents one remedy. UAV platforms excel in this regard because they accommodate multiple sensors that yield multifaceted data. The central question concerns which imagery types deliver the best results for urban classification tasks.

For this reason, the present study examined the relative priority of various UAV-derived images to support robust land cover mapping tailored for urban environmental applications. The methodology involved the following stages: (1) multispectral data collection via UAV along with production of vegetation indices and topographic maps; (2) assessment of suitable images and variables for urban land cover classification through OBIA and random forest (RF) techniques; and (3) subsequent reclassification of land cover using a reduced variable set to better determine the practicality and precision of UAV imagery in this domain.

Materials and Methods

Target site and research processes

The entire grounds of Changwon University, located in Changwon, Gyeongsangnam-do, South Korea, were selected as the study site. This campus features a wide variety of land cover classes compressed into a limited space, providing an excellent setting to test urban land cover mapping derived from UAV imagery **(Figure 1)**. The surveyed UAV area formed

© 2026 The Author(s). | Published by Agro Intelligence Research Press

a rectangular zone measuring 623 m × 1138 m, extending slightly beyond the university boundaries. The surrounding terrain is hilly, averaging around 600 m above sea level. University structures are mostly five to eight stories tall and include expansive walkways built from sidewalk blocks, roads with vehicle traffic and paved surfaces, and extensive landscaping with lawns and trees.

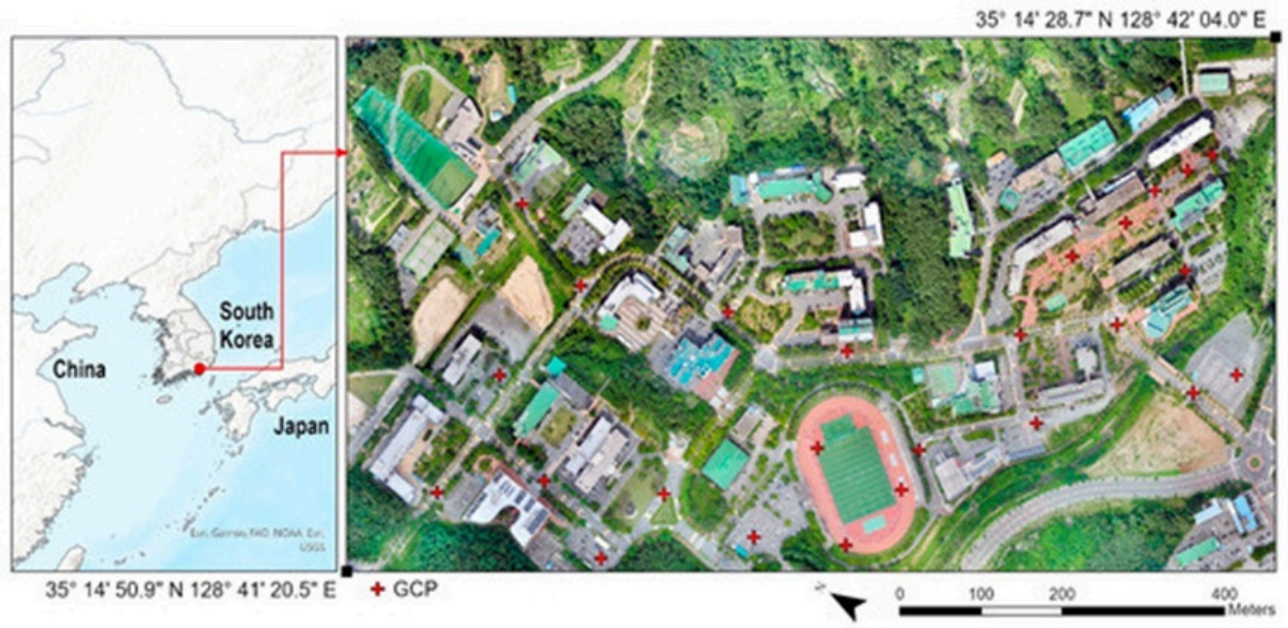


Figure 1. Study area (original UAV image-RGB).

The overall workflow consists of five core phases **(Figure 2)**: data acquisition, image preprocessing, image segmentation, classification, and accuracy assessment. Primary data collection included UAV operations to acquire ground control points (GCPs) essential for orthoimage production and accurate image overlap. Preprocessing steps focused on pinpointing the most useful images and variables for urban land cover discrimination. To achieve this, variations in data scales were removed to ensure uniform weighting across all images (further explained in Section 2.2). Objects were then formed by merging pixels with comparable attributes via segmentation. Training samples were developed and fed into an RF classifier using every variable derivable from the UAV dataset, enabling calculation of variable importance. This step highlighted the strongest images and variables for urban classification, after which the model was retrained on the trimmed dataset. Final stages involved accuracy evaluation and validation to determine the overall value of UAV imagery combined with OBIA for urban land cover mapping.

© 2026 The Author(s). | Published by Agro Intelligence Research Press

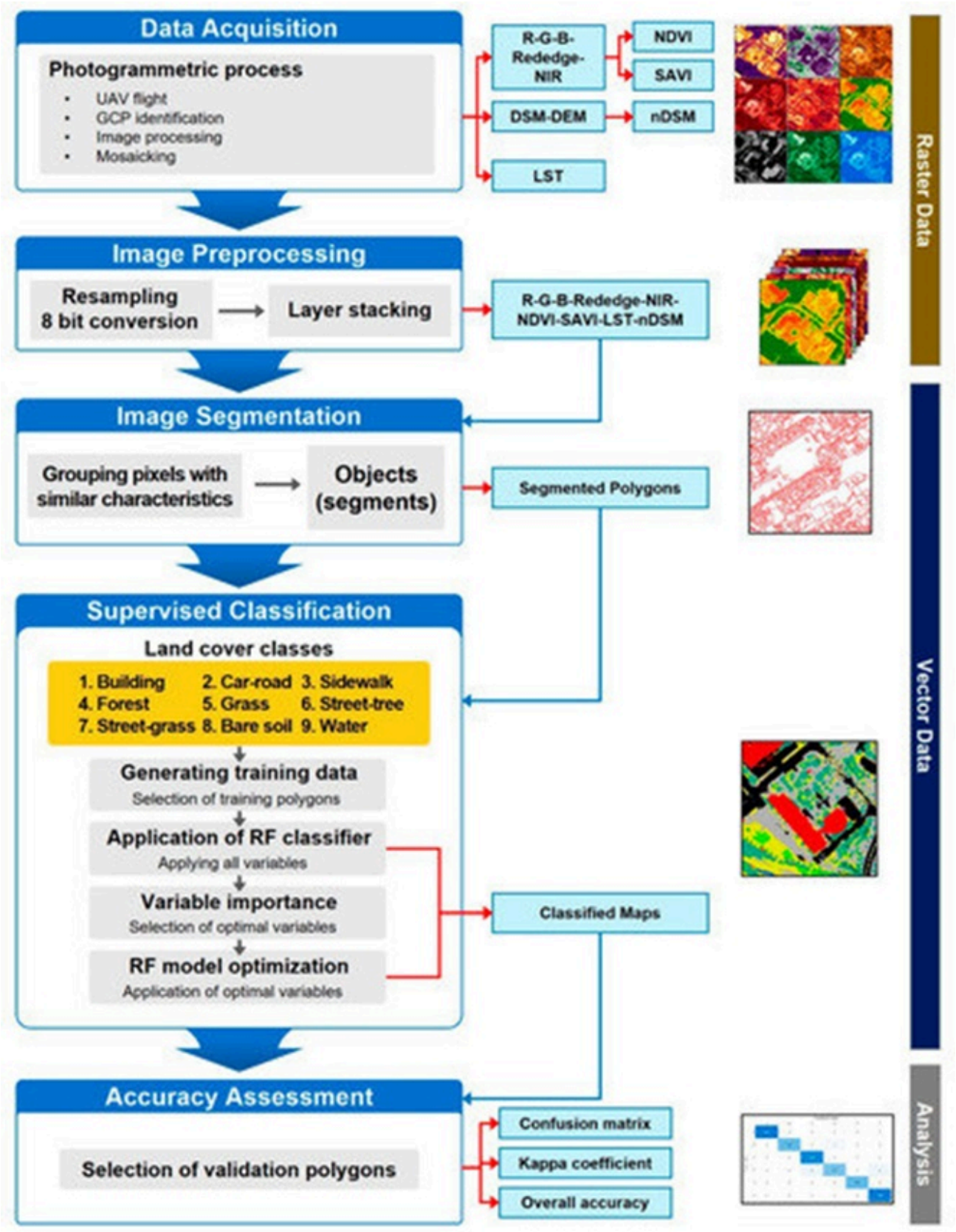


Figure 2. Conceptual diagram of data acquisition, preprocessing, segmentation, classification, and validation steps implemented to derive an object-based land cover map for an urban environment from UAV imagery.

© 2026 The Author(s). | Published by Agro Intelligence Research Press

UAV image acquisition and preprocessing

The UAV utilized in this research was a fixed-wing eBeeX model manufactured by Sensefly (Cheseaux-sur-Lausanne, Switzerland), with an approximate weight of 1.4 kg and a wingspan of 116 cm. This aircraft can fly at speeds of 40–110 km·h−1 and remain airborne for up to 90 min. It accommodates multiple sensor options, such as RGB, thermal infrared, and 5-band multispectral sensors, and includes integrated real-time/post-processed kinematic (RTK/PPK) capabilities. For this study, the Duet-T (RGB + Thermal) and RedEdge-MX (Red, Green, Blue, Rededge, NIR) sensors were employed. Data collection occurred on 21 June, 2021, during a completely clear day with no cloud cover. Flight parameters were configured as follows: the RedEdge-MX sensor operated at a ground sample distance (GSD) of 13 cm·pixel−1, while the Duet-T sensor used a GSD of 20 cm·pixel−1. Vertical and horizontal overlap were both maintained at 75%. Additionally, 25 ground control points (GCPs) displayed in **Figure 1** were placed to support aerial triangulation of the drone imagery.

The acquired UAV photographs were processed into orthoimages using Pix4D Mapper v.4.4.12 (Prilly, Switzerland). This produced separate layers comprising Red, Green, Blue, RedEdge, and NIR bands, along with a digital surface model (DSM), a digital elevation model (DEM), and land surface temperature (LST). Radiometric correction for the five-band RedEdge-MX imagery was achieved using a calibrated reflectance panel and a downwelling light sensor. Panel images captured before and after each flight enabled correction of UAV image reflectance values against known reference values in post-processing. The downwelling light sensor, mounted on the UAV's upper surface and oriented upward, continuously measured ambient light during flights and contributed to reflectance correction alongside the panel images.

Furthermore, the normalized difference vegetation index (NDVI) and soil-adjusted vegetation index (SAVI) were computed using **Eqs. 1 and 2**. NDVI serves as a vegetation health indicator derived from red and NIR bands, with higher values indicating denser live vegetation. SAVI, on the other hand, adjusts NDVI to account for soil brightness effects in sparsely vegetated zones. For Landsat-derived SAVI, a soil brightness correction factor (L) of 0.5 is typically applied to handle a wide range of land cover types when modifying the NIR-to-red ratio [40]. By subtracting the DEM (which captures bare-surface elevation) from the DSM, a normalized digital surface model (nDSM) was created to isolate the height of above-ground natural features. Incorporating nDSM into classification is expected to enhance the separation of buildings and trees across the landscape.

$$\mathrm{NDVI} = \frac{\mathrm{NIR} - \mathrm{Red}}{\mathrm{NIR} + \mathrm{Red}} \quad (1)$$

$$\mathrm{SAVI} = \frac{\mathrm{NIR} - \mathrm{Red}}{\mathrm{NIR} + \mathrm{Red} + \mathrm{L}} \times (1 + \mathrm{L}) \quad (2)$$

All resulting images were resampled to a uniform GSD of 15 cm·pixel−1 and aligned with the multispectral imagery to better detect street grass areas established between roads for landscaping. Given that the various UAV-derived images used inconsistent units—for example, meters for nDSM and degrees Celsius (°C) for LST—the data required standardization. Following recommendations by Immitzer *et al.* [41] and Luca *et al.* [30], numerical scales were normalized to a shared range at this stage. This step minimized the impact of potential outliers in subsequent segmentation and classification while ensuring equal weighting across all variables. Consequently, each input layer was linearly stretched to an 8-bit scale ranging from 0 to 255. In the end, a layer stack operation was performed to combine RGB, RedEdge, NIR, NDVI, SAVI, LST, and nDSM into a single unified raster dataset for image segmentation.

© 2026 The Author(s). | Published by Agro Intelligence Research Press

Image segmentation and object creation

Image segmentation involves partitioning raster pixels with similar spectral and geometric properties into coherent objects. The shape and dimensions of the object are influenced by the chosen object-based weighting parameters [42]. This approach allows computation of mean pixel statistics for neighboring pixel clusters and clearly defines object membership. Segmentation transforms detailed raster areas into broader, continuous regions while preserving essential feature information, rather than treating data as isolated pixels [43]. As a result, the effectiveness of OBIA hinges on high-quality segmentation, with final classification performance closely tied to these outputs. In this work, ArcGIS Pro v.2.8 from ESRI (Redlands, CA, USA) was used to perform segmentation using a composite image formed by stacking nine orthoimage layers. Key considerations during segmentation include the balance of weights for object generation, which can be tuned by varying spectral and spatial detail settings from 1 to 20. Spectral detail controls differentiation based on color and reflectance traits; for instance, increasing this value in forested areas improves separation among tree species. Spatial detail governs separation according to geometric attributes, with higher settings better suited for compact, densely grouped features [44]. Although segmentation reduces computational demands by simplifying spectral variation and shrinking file sizes associated with high-resolution data, the link between weight inputs and segmentation outcomes remains complex. Analysts must therefore rely on iterative testing to establish optimal parameters [45, 46]. Lowering either weight reduces data complexity and storage requirements. Typically, combinations featuring strong spectral detail paired with weaker spatial detail are favored for faster execution. Smaller objects can be merged into neighboring similar segments by defining an appropriate minimum segment size threshold. In practice, spectral detail was first tested from 10 to 20 at intervals of 5, while spatial detail was also stepped in units of 5. These were then refined at increments of 1. The minimum segment size was progressively tested from 20 to 60 in steps of 10, with undersized objects merged with adjacent ones until suitable final parameters were identified.

Land cover classification via random forest

Land cover maps serve as essential baseline information for urban-scale studies. Accordingly, nine classes were defined to adequately represent the urban landscape **(Figure 2)**: buildings, car-road, sidewalk, forest, grass, street-tree, street-grass, bare soil, and water. Here, street-tree and street-grass denote vegetation elements specifically used for landscaping. Road areas were further split into vehicle and pedestrian zones, while vegetation categories (forests, street trees, grass, and street grass) were treated separately. This subdivision was necessary because vehicle zones generate air pollutants such as fine dust and NOx, unlike pedestrian sidewalks. Additionally, in accordance with the Ministry of Environment of South Korea's guidelines, any street-tree or street-grass patches that fell below a minimum area threshold were reclassified as road cover. These specific categories were retained for their multiple benefits, including reducing fine dust, creating wind corridors, and mitigating urban heat.

Statistical attributes extracted for each object from the UAV imagery included: count, area, mean, max, range, standard deviation (STD), sum, variety, majority, minority, median, percentile (PCT), and nearby mean STD (NMS). This yielded a total of 126 variables, obtained by deriving 14 statistical measures for every image layer per object. The study aimed to differentiate street trees from spectrally similar forests and street-grass from general grass areas. While forests and grass are usually bordered by spectrally consistent surroundings, street-tree and street-grass patches are adjacent to non-vegetated surfaces (roads, sidewalks, buildings), creating greater spectral contrast in their vicinity. The NMS variable was therefore introduced to compare local mean values within a 3 m radius using standard deviation.

Training polygons for supervised classification ranged in size from 1000 to 5000 for the eight non-water classes. Only 165 water polygons were collected due to extensive vegetation along rivers. All polygons were manually digitized via on-screen interpretation, ensuring balanced representation across land cover types and accounting for varying illumination and color tones within the study site.

RF refers to the ensemble machine learning method introduced by Breiman [47], which combines numerous decision trees via bootstrap aggregation (bagging). It integrates multiple base classifiers trained on varied subsets of the data—for

© 2026 The Author(s). | Published by Agro Intelligence Research Press

example, some trees use the full sample set while others omit specific instances. Although single trees are prone to training data noise, the ensemble voting process, which decreases inter-tree correlation, yields robust performance against noise [48, 49].

Despite its strengths, the RF classifier, like many machine learning techniques, offers limited direct insight into relationships between independent and dependent variables. This can make variable selection in OBIA subjective and laborious when many predictors are involved [50, 51]. Variable importance metrics were therefore applied to identify the most influential predictors, allowing for streamlined variable selection and model optimization.

Adequate training sample collection is critical for RF. Congalton and Green [52] stressed the necessity of sufficient samples to support reliable accuracy evaluation. Given the unequal area distribution of land cover classes, proportionate sampling was implemented to avoid statistical bias. Of the 254,456 total image objects, 22,353 (8.8%) were selected as training samples. Within the training set, 30% was reserved for validation. RF parameters were tuned as follows: number of trees between 100 and 1000, maximum tree depth between 5 and 10, and minimum leaf size between 1 and 3. After experimentation, optimal settings were established at 500 trees, a maximum depth of 10, and a minimum leaf size of 2. Variable importance was assessed, less useful variables were removed, the model was retrained, and performance was compared against the baseline model using the same settings.

Random points for accuracy assessment of the final land cover map are illustrated in **Figure 3**. A confusion matrix was constructed to compute producer's accuracy, user's accuracy, and overall accuracy. Verification involved 500 randomly distributed points that were visually interpreted against the original UAV imagery.



Figure 3. Random point locations for accuracy verification.

Results and Discussion

Results of UAV flight

© 2026 The Author(s). | Published by Agro Intelligence Research Press

UAV data gathering resulted in 5925 images captured by the RedEdge-MX sensor across RGB, RedEdge, and NIR bands. The Duet-T sensor contributed an additional 1132 RGB and LST images. **Figure 4** illustrates the mosaicked products created from the gathered images, yielding nine images that underwent evaluation. Following geometric correction with GCPs, Duet-T images recorded RMSE values of 0.033 m in the x-direction and 0.048 m in the y-direction. RedEdge-MX images recorded RMSE values of 0.056 m in the x-direction and 0.054 m in the y-direction.

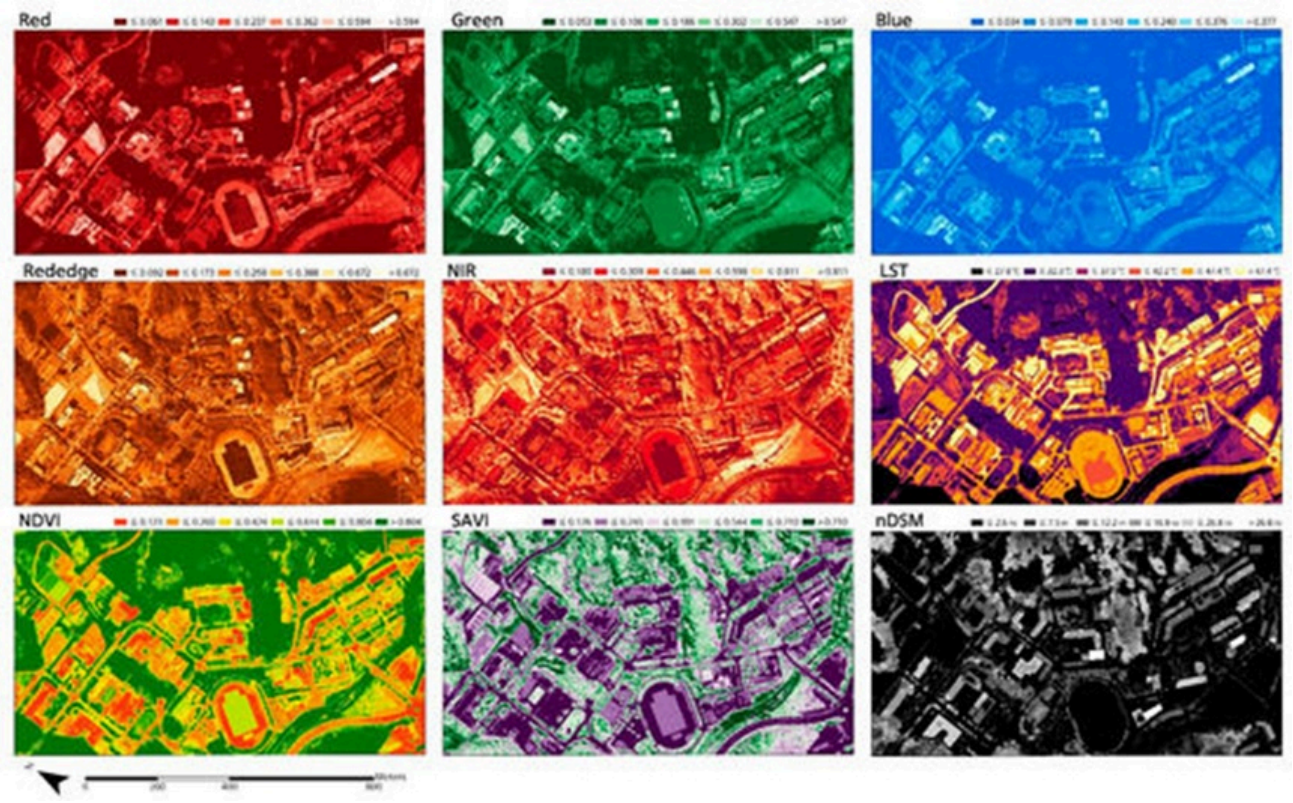


Figure 4. UAV image production results.

Optimal image segmentation weight

In determining segmentation weights, a spectral detail setting of 10 resulted in blurred edges between the road and grass zones **(Figure 5)**. With spectral detail at 15, some regions failed to clearly separate the road from the sidewalk. At a spectral resolution of 20, objects showed excessive fragmentation even within the same land cover group. While class boundaries were clearly defined, the small object sizes increased the risk of image noise. At spectral or spatial detail levels of 15 or higher, car-road became separable from sidewalk, but asphalt car-road remained indistinct from bare-soil areas made of gravel. Additional increases in spectral detail were located at settings where all land cover class borders appeared distinct at a spectral detail of 18 paired with a spatial detail of 10, avoiding overly minute objects. Applying a minimum segment size of 40 achieved balanced object dimensions, particularly with sharp street-grass outlines, making this the adopted weight.

© 2026 The Author(s). | Published by Agro Intelligence Research Press

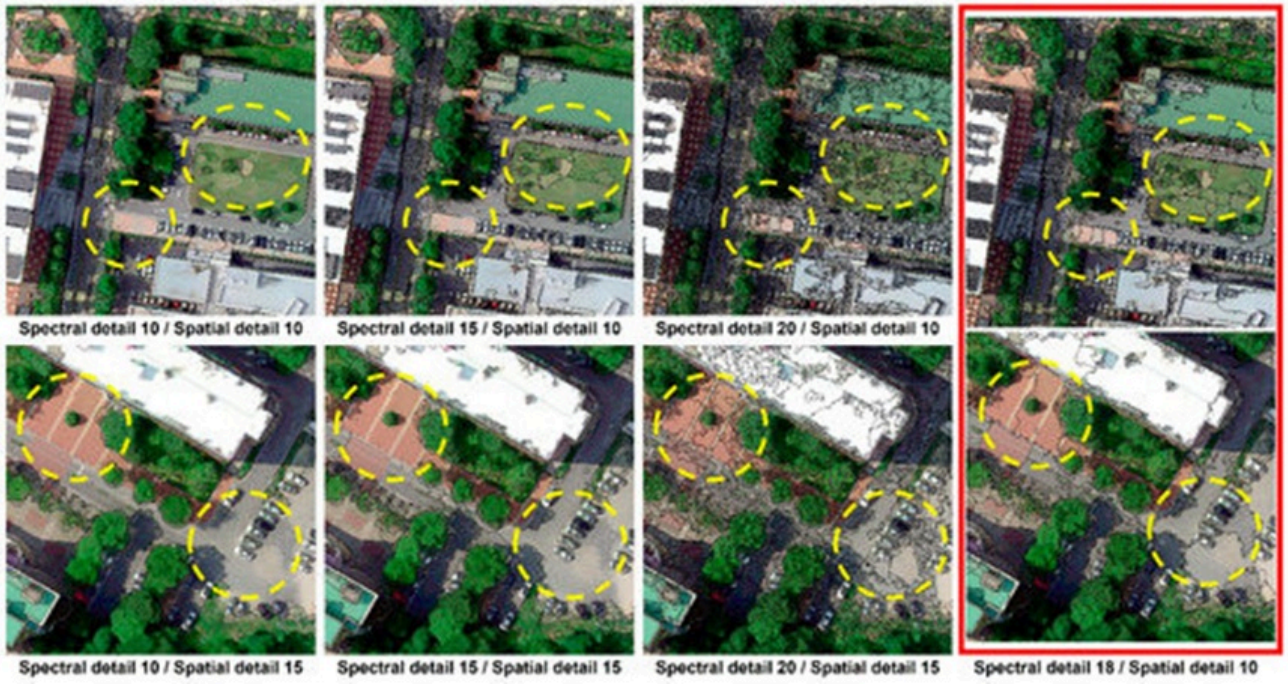
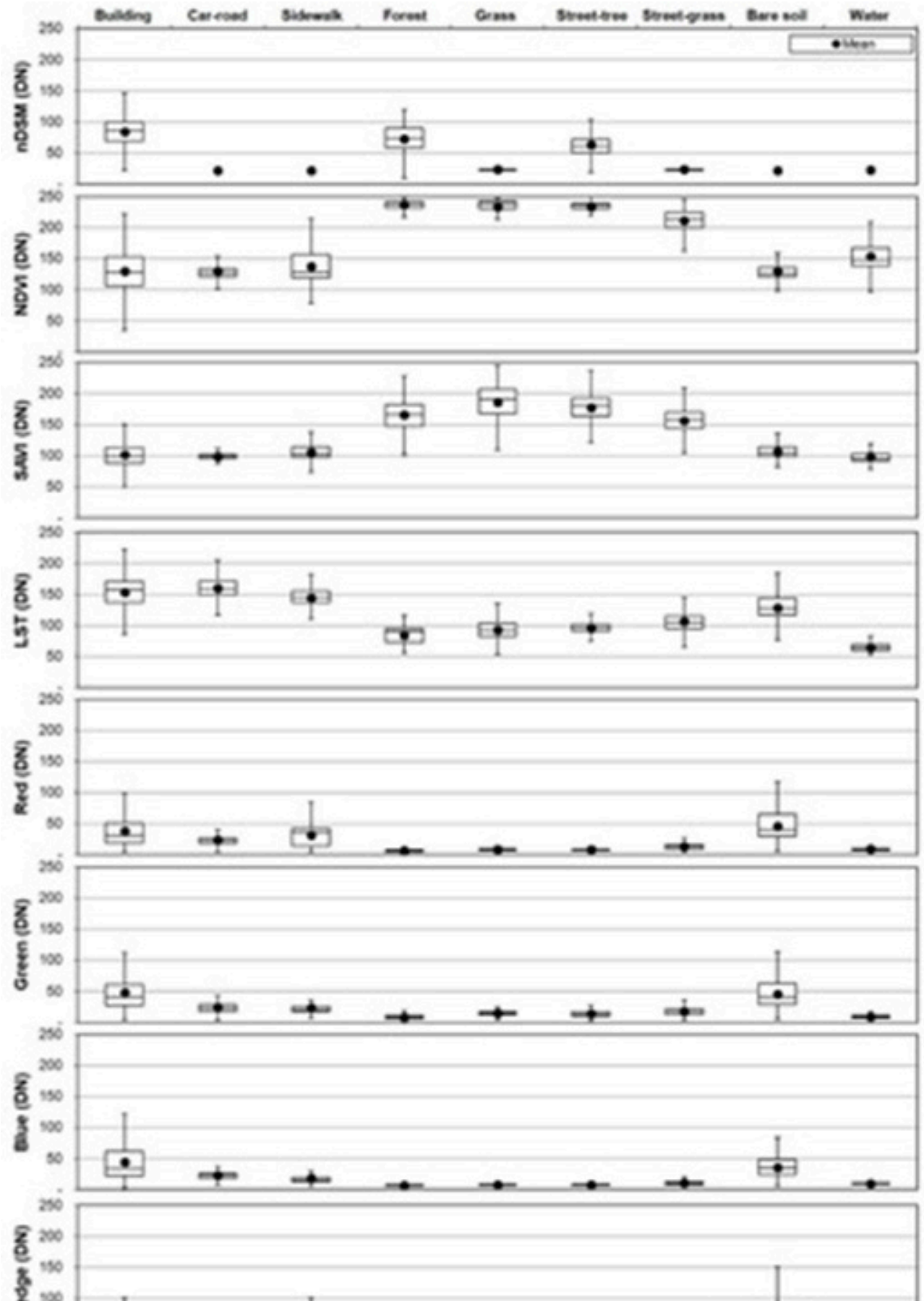


Figure 5. Image segmentation results.

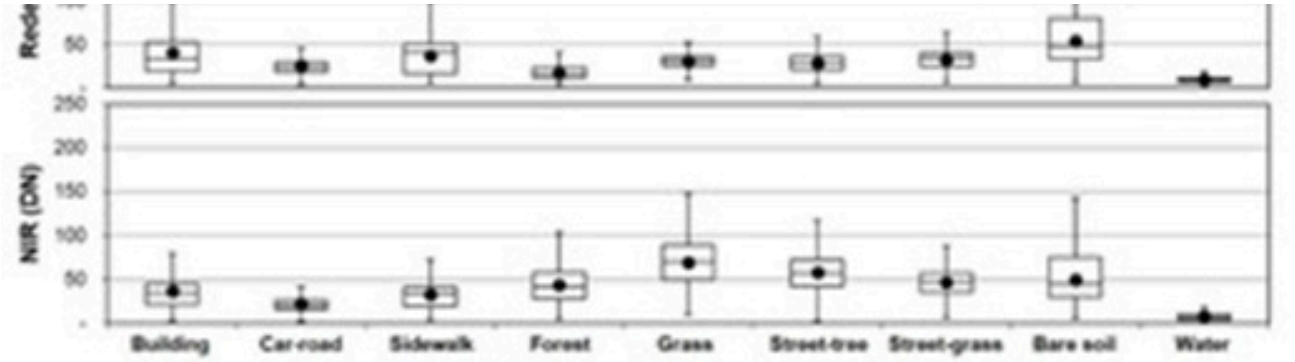
Land cover map classification results

Figure 6 depicts the trait distributions of training samples by class. Regarding nDSM, interquartile ranges were 69–100 for buildings, 58–90 for forest, and 51–72 for street trees, with other classes showing virtually no variation. This height-based trait enabled strong isolation of buildings, forests, and street trees from the remaining cover. NDVI and SAVI showed noticeable elevations across vegetation groups. Vegetation NDVI interquartile range covered 231–243, exceeding the top third quartile of non-vegetation classes (below 167). SAVI vegetation interquartile range spanned 144–207, surpassing the highest non-vegetation third quartile (below 114). Street-grass NDVI varied more widely from mixed grass-soil exposure. Non-vegetation categories overlapped heavily, so NDVI and SAVI supported coarse vegetation-versus-non-vegetation splits but offered limited help in distinguishing finer elements such as car roads, sidewalks, and bare soil. LST interquartile ranges per class included 137–171 (building), 150–172 (car-road), 137–155 (sidewalk), 73–95 (forest), 83–104 (grass), 91–102 (street-tree), 95–115 (street-grass), 117–144 (bare soil), and 60–69 (water). Water separated distinctly, with vegetation (forest, grass) also low. Human-made covers, such as buildings and roads, registered higher LST, and bare soil extended across the vegetation-to-artificial gradient. Red, Green, and Blue bands had largely overlapping boxplots for car-road, sidewalk, and bare soil, except for the blue band. Blue band interquartile ranges were 19–26 (car-road), 13–20 (sidewalk), and 24–48 (bare soil), providing modestly improved distinction over red and green. NIR and rededge showed broad overlaps across classes, except for water. Car-road, primarily black asphalt, produced narrower boxplots than multicolored sidewalk paving.

© 2026 The Author(s). | Published by Agro Intelligence Research Press



© 2026 The Author(s). | Published by Agro Intelligence Research Press



acquisition under a high sun angle best limits shadow influence for LST use. Blue band led single-wavelength importance by better isolating car-road, sidewalk, and bare soil. Statistical metric importance counts were PCT75 (6), mean (6), NMS (5), majority (5), median (5), max (5), min (4), minority (3), and STD (1). nDSM emphasized median, PCT75, and mean; NDVI stressed mean, PCT75, and median. NMS for street-tree versus street-grass separation relied most on nDSM and green.

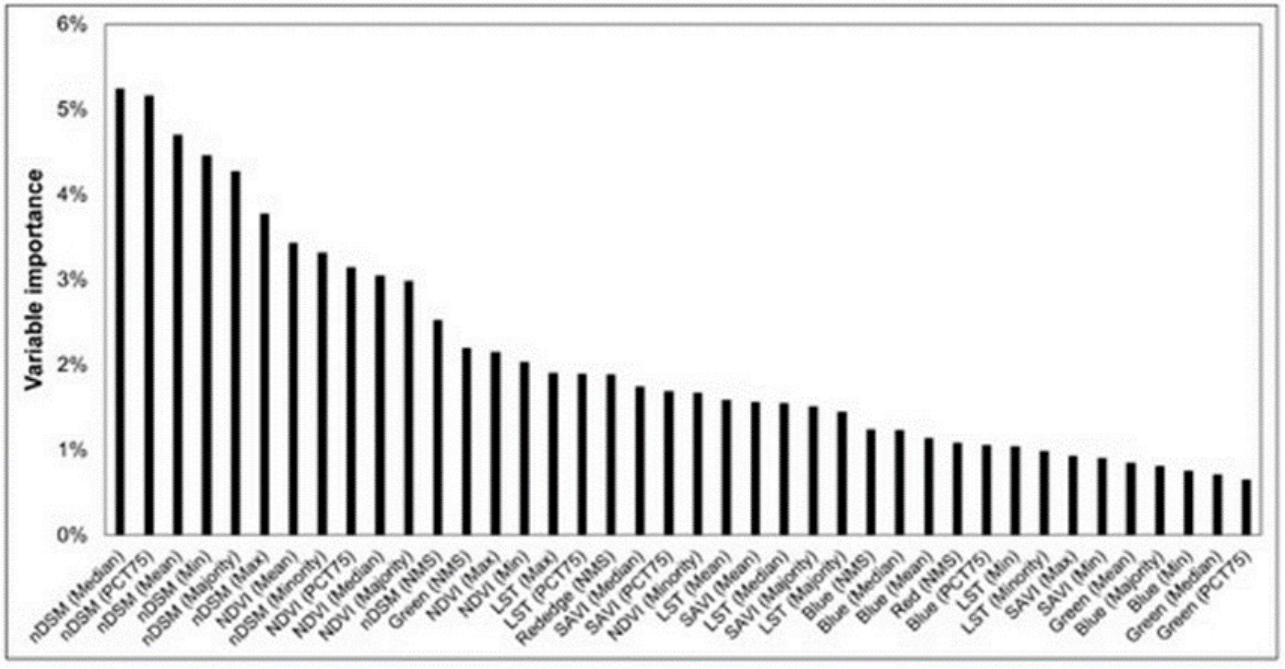


Figure 7. The 40 most important variables out of 126 were assessed.

Importance scores enabled trimming to six layers (nDSM, NDVI, SAVI, LST, blue, green) plus seven metrics (PCT75, mean, NMS, median, majority, max, min). Full-area model outputs appear in **Figure 8**. The 126-variable model gave area shares of forest (19.2%) > car-road (16.8%) > street-grass (16.6%) > street-tree (14.8%) > sidewalk (13.5%) > building (11.5%) > grass (5.3%) > bare soil (2.2%) > water (0.1%). The reduced optimized model produced forest (19.1%) > car-road (17.6%) > street-grass (16.4%) > street-tree (14.7%) > sidewalk (12.2%) > building (11.6%) > grass (5.8%) > bare soil (2.5%) > water (0.1%). Proportions remained comparable (differences ≤ 1%), with sidewalk as the main exception, confirming a little overall shift across fewer variables.

© 2026 The Author(s). | Published by Agro Intelligence Research Press

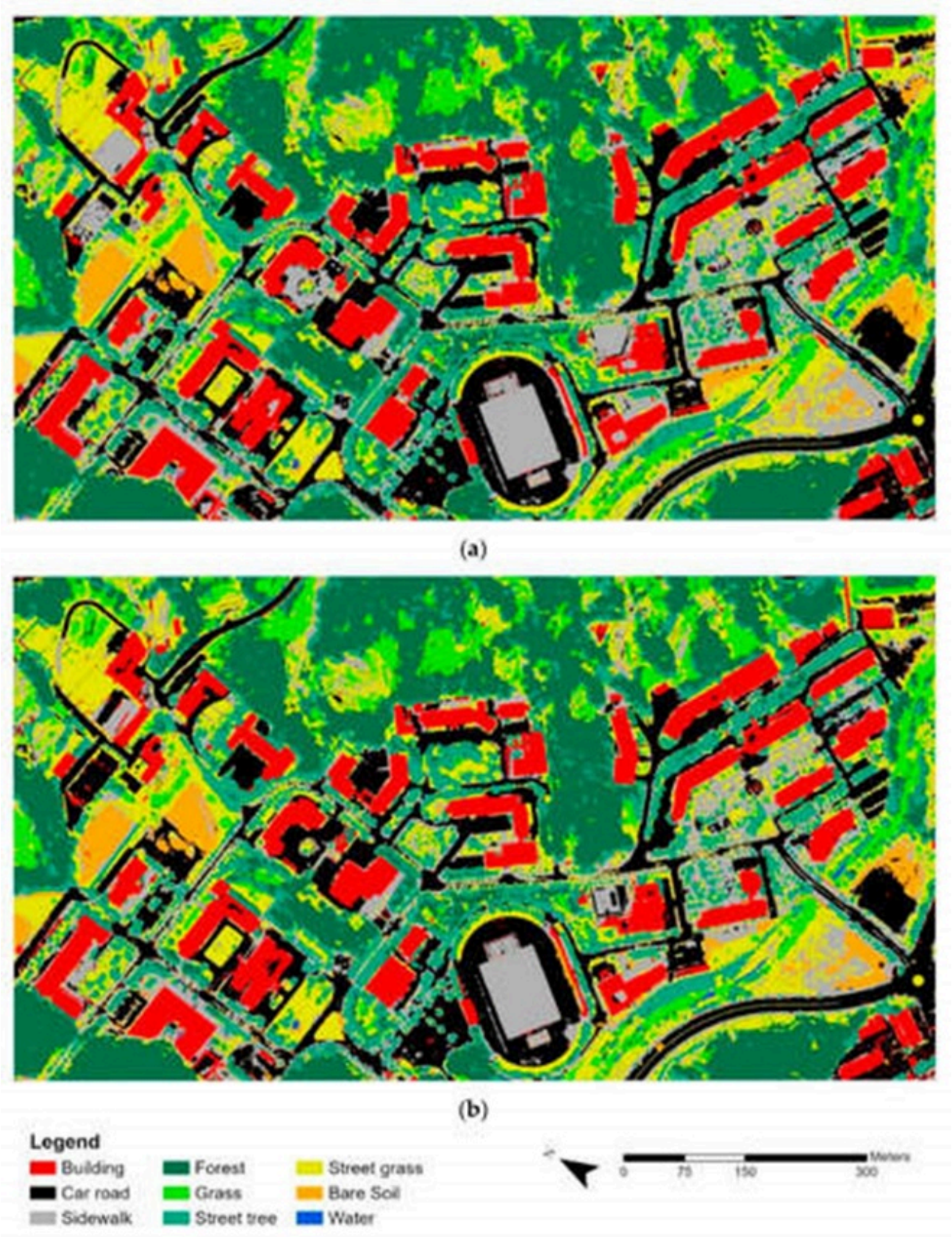


Figure 8. Results of applying the RF model to the entire target sites: (a) Initial RF with 126 variables, and (b) Optimized RF with a reduced number of variables.

© 2026 The Author(s). | Published by Agro Intelligence Research Press

A detailed review indicated effective separation between forests and street trees. Water, despite a tiny area and few samples, was classified reliably. Built features like buildings and car-roads performed well, and car-road/sidewalk separation succeeded, though occasional car-road-to-sidewalk errors occurred. Remote sensing often struggles with shadows, requiring greater effort in detection and correction [53, 54]. Examples included forest paths labeled as sidewalks, nearby grass labeled as street grass, and bare soil frequently assigned to sidewalks.

Accuracy verification

Verification yielded a full-variable initial RF with a Kappa of 0.728 (76.0% overall accuracy). The optimized RF reached Kappa 0.721 (75.4% overall accuracy), with negligible drop after variable reduction **(Tables 1 and 2)**. Post-optimization, users' accuracy varied within ± 3% for building, car-road, sidewalk, forest, grass, street-tree, and street-grass. Water gained 4.9%. Sidewalk-to-bare-soil confusion rose, cutting sidewalk users' accuracy by 13.8%. Producer's accuracy stayed within ± 3% for building, forest, street-tree, bare soil, and water. Sidewalk and street-grass dropped 7.5% and 6.0%; grass and car-road rose 7.0% and 5.6%. Variable cuts affected buildings, forests, and street trees minimally, matching earlier nDSM and NDVI success for those classes [55-57]. Vanhuysse *et al.* [58] observed better building performance, both quantitatively and qualitatively, with nDSM input. Here, retained high-ranking nDSM and NDVI explain the stable performance for these categories after trimming.

Table 1. Confusion matrix for the initial RF.

Classification	Reference data								
	Building	**Car-Road**	**Sidewalk**	**Forest**	**Grass**	**Street-Tree**	**Street-Grass**	**Bare Soil**	**Water**
Building	46	2	1	0	0	0	0	0	0
Car-road	0	38	3	0	0	0	0	2	0
Sidewalk	1	10	72	0	1	0	2	24	0
Forest	0	0	0	43	2	4	0	0	0
Grass	0	0	0	2	48	0	12	0	0
Street-tree	0	0	1	11	0	45	0	0	0
Street-grass	1	4	1	0	20	2	35	8	1
Bare soil	0	0	1	0	0	0	0	18	0
Water	0	0	1	0	0	0	1	2	35
Producer Acc. (%)	95.8	70.4	90.0	76.8	67.6	88.2	70.0	33.3	97.2
User Acc. (%)	93.9	88.4	65.5	87.8	77.4	78.9	48.6	94.7	89.7
Overall Acc. (%)	76.0			**Kappa coefficient**			0.728		

Table 2. Confusion matrix for the optimized RF.

Classification	Reference data								
	Building	**Car-Road**	**Sidewalk**	**Forest**	**Grass**	**Street-Tree**	**Street-Grass**	**Bare Soil**	**Water**
Building	46	2	2	0	0	0	0	0	0
Car-road	0	41	5	0	0	0	0	2	0

© 2026 The Author(s). | Published by Agro Intelligence Research Press

Sidewalk	0	8	66	0	0	0	3	25	0
Forest	0	0	0	43	1	4	0	0	0
Grass	0	0	0	1	53	0	14	0	0
Street-tree	1	0	1	12	0	44	0	0	0
Street-grass	1	3	1	0	17	3	32	10	1
Bare soil	0	0	4	0	0	0	0	17	0
Water	0	0	1	0	0	0	1	0	35
Producer Acc. (%)	95.8	75.9	82.5	76.8	74.6	86.3	64.0	31.5	97.2
User Acc. (%)	92.0	85.4	64.7	89.6	77.9	75.9	47.1	81.0	94.6
Overall Acc. (%)		75.4			**Kappa coefficient**		0.721		

Optimized RF kept building and water above 90% of users' and producers' accuracy. nDSM drove building identification, and LST created the largest gap for water **(Figure 6)**. NDVI supported strong vegetation results via limited boxplot overlap. Merging car-road and sidewalk as a road yielded 89.6% producer's and 80.0% user's accuracy, matching the literature range (75%–95%) [57, 59-61]. Sidewalk over-prediction reduced its user's accuracy to 65.7%. Varied sidewalk block colors (beige, red, green, gray) caused bare soil mislabeling as sidewalk **(Figure 9)**, with 46% of bare soil points reassigned and producer's accuracy at 31.5%. Combining forest and street trees into a single tree class boosted accuracies to 97.2% for users and 96.3% for producers. Separate classification reduced performance due to inter-subclass swaps, linked to tree shadows during visual checks. Future inclusion of forest-type maps could lessen such issues.

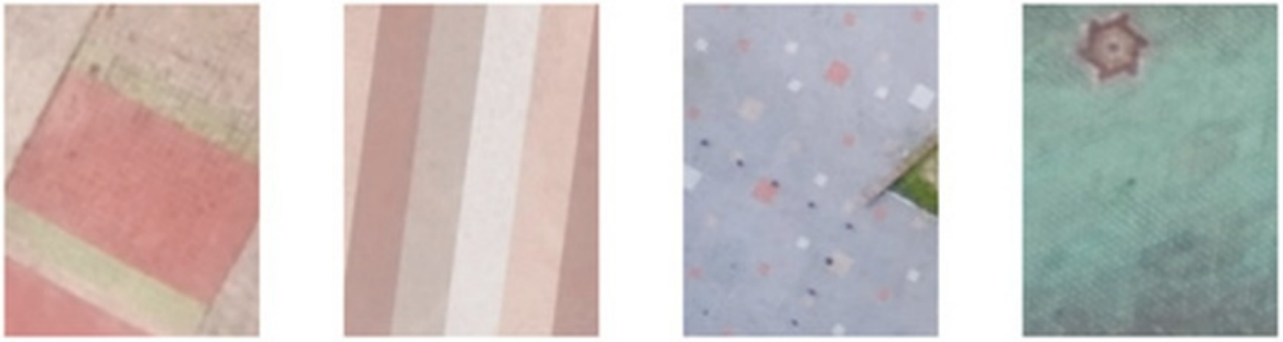


Figure 9. Example of sidewalk block types in the target site.

Conclusion

Land cover maps provide essential spatial information vital for assessing and studying urban environments. Yet, their use remains restricted in small- and medium-scale zones due to insufficient temporal resolution, lower precision, and higher production costs. This research addressed those constraints by examining suitable imagery from UAV platforms for building land cover maps and validating the practicality of the classification approach. The main outcomes achieved are outlined below.

Nine images generated from UAV sources supported OBIA: red, green, blue, RedEdge, NIR, LST, NDVI, SAVI, and nDSM. The optimal segmentation weights consisted of spectral detail 18, spatial detail 10, and a minimum segment size of 40. The initial RF training included 126 variables and derived importance rankings from the top 40, with the leading variables ranked as nDSM > NDVI > LST > SAVI > blue > green > red > rededge. nDSM proved useful for separating

© 2026 The Author(s). | Published by Agro Intelligence Research Press

buildings from trees. In contrast, NDVI separated vegetation from non-vegetation groups and performed markedly better than SAVI, which aims to reduce soil brightness effects (a highly inconsistent trait). LST importance values ranked between 16th and 33rd. Although earlier efforts focused primarily on multispectral bands and vegetation indices for land cover mapping, findings demonstrated that LST imagery can be effective for urban land cover classification. It served as a key element in separating the car road from the sidewalk and from the water. For best results with LST imagery, capture around noon during summer is preferable, as shadow impacts diminish under peak solar elevation. Among single-wavelength bands, blue achieved the strongest importance level for isolating car-road, sidewalk, and bare soil. Lastly, regarding NMS applied to differentiate street trees from street grass, nDSM and green bands showed higher priority.

Comparison between the full 126-variable initial RF land cover outcomes and the optimized RF after variable trimming showed a 1.3% difference in total area proportions. Notably, classification patterns across the study zone exhibited no major alterations even with fewer variables. Accuracy checks indicated a Kappa coefficient of 0.728 for the initial RF, compared with 0.721 for the optimized RF. Review of per-class accuracy shifts confirmed that buildings, forests, and street trees experienced negligible effects, likely due to the strong contributions of nDSM and NDVI, which ranked highest in importance. Treating the car-road and sidewalk together as a single road (a common practice in comparable research) produced producer and user accuracies of 89.6% and 80.0%, in line with values from other studies. However, bare soil was often mislabeled as a sidewalk because the sidewalk paving blocks were multicolored. Merging forest and street trees into a single tree category increased user and producer accuracies to 97.2% and 96.3%, respectively. Accuracy declined, though, upon splitting them back into forest and street trees. On-screen review indicated that tree shadows exerted considerable influence. Therefore, adding forest-type maps as supporting information could reduce this issue.

Gathering imagery with UAVs involves fewer spatiotemporal restrictions than with satellite or conventional aerial platforms. It further enables the acquisition of higher-quality information at a lower cost and effort than processing. The application of object-based classification techniques to UAV data is expected to advance urban environmental investigations. Nevertheless, because this work produced a land cover map for a single time period, additional investigations are required to test time-series land cover map development and to identify other strategies that enhance classification precision. Typically, forests require consideration of minimum area and canopy coverage thresholds, yet these were not addressed here. Subsequent studies should address this limitation.

Acknowledgements

None

Conflict of interest

None

Financial support

This result was supported by “Regional Innovation Strategy (RIS)” through the National Research Foundation of Korea (NRF) funded by the Ministry of Education (MOE) (2021RIS-003) and the National Research Foundation of Korea (NRF) grant funded by the Korean government (MSIT) (No. NRF-2019R1F1A1063921).

Ethics statement

None

Received: 30 Sep 2024 Revised: 05 Dec 2024 Accepted: 20 Dec 2024

© 2026 The Author(s). | Published by Agro Intelligence Research Press

Published online: 25 November 2026

Rights and permissions

Open Access The author(s) retain copyright. This article is licensed under the Creative Commons Attribution-NonCommercial-ShareAlike 4.0 International License. It may be shared and adapted for non-commercial purposes with appropriate attribution, an indication of changes, and distribution of adaptations under the same license. Third-party material may be subject to separate terms identified in its credit line. View the license at https://creativecommons.org/licenses/by-nc-sa/4.0/.

References

1. Song B, Park K. Temperature trend analysis associated with land-cover changes using time-series data (1980–2019) from 38 weather stations in South Korea. Sustain Cities Soc. 2021;65:102615.

2. De Castro AI, Torres-Sánchez J, Peña JM, Jiménez-Brenes FM, Csillik O, López-Granados F. An automatic random forest-OBIA algorithm for early weed mapping between and within crop rows using UAV imagery. Remote Sens. 2018;10:285.

3. Kim EJ, Won J, Kim J. Is Seoul walkable? Assessing a walkability score and examining its relationship with pedestrian satisfaction in Seoul, Korea. Sustainability. 2019;11:6915.

4. Takahashi Miyoshi G, Imai NN, Garcia Tommaselli AM, Antunes de Moraes MV, Honkavaara E. Evaluation of hyperspectral multitemporal information to improve tree species identification in the highly diverse Atlantic Forest. Remote Sens. 2020;12:244.

5. Song B, Park K. Analysis of spatiotemporal urban temperature characteristics by urban spatial patterns in Changwon City, South Korea. Sustainability. 2019;11:3777.

6. Yoo SH, Lee JS, Bae JS, Sohn HG. Automatic generation of land cover map using residual U-Net. KSCE J Civ Environ Eng Res. 2020;40:535–46.

7. Kim J, Song Y, Lee WK. Accuracy analysis of multi-series phenological landcover classification using U-Net-based deep learning model—focusing on the Seoul, Republic of Korea. Korean J Remote Sens. 2021;37:409–18.

8. Scaioni M, Longoni L, Melillo V, Papini M. Remote sensing for landslide investigations: An overview of recent achievements and perspectives. Remote Sens. 2014;6:9600–52.

9. Van Iersel W, Straatsma M, Addink E, Middelkoop H. Monitoring height and greenness of non-woody floodplain vegetation with UAV time series. ISPRS J Photogramm Remote Sens. 2018;141:112–23.

10. Song B, Park K. Verification of accuracy of unmanned aerial vehicle (UAV) land surface temperature images using in-situ data. Remote Sens. 2020;12:288.

11. Park G, Park K, Song B. Spatio-temporal change monitoring of outside manure piles using unmanned aerial vehicle images. Drones. 2021;5:1.

12. Song B, Park K. Detection of aquatic plants using multispectral UAV imagery and vegetation index. Remote Sens. 2020;12:387.

13. Uysal M, Toprak AS, Polat N. DEM generation with UAV photogrammetry and accuracy analysis in Sahitler Hill. Measurement. 2015;73:539–43.

14. Ferrer-González E, Agüera-Vega F, Carvajal-Ramírez F, Martínez-Carricondo P. UAV photogrammetry accuracy assessment for corridor mapping based on the number and distribution of ground control points. Remote Sens. 2020;12:2447.

15. Prado Osco L, Marques Ramos AP, Roberto Pereira D, Akemi Saito Moriya É, Nobuhiro Imai N, Takashi Matsubara E, et al. Predicting canopy nitrogen content in citrus trees using random forest algorithm associated to spectral vegetation indices from UAV imagery. Remote Sens. 2019;11:2925.

16. Siebert S, Teizer J. Mobile 3D mapping for surveying earthwork projects using an unmanned aerial vehicle (UAV) system. Autom Constr. 2014;41:1–14.

17. Su TC. A study of a matching pixel by pixel (MPP) algorithm to establish an empirical model of water quality mapping, as based on unmanned aerial vehicle (UAV) images. Int J Appl Earth Obs Geoinf. 2017;58:213–24.

18. Nex F, Remondino F. UAV for 3D mapping applications: A review. Appl Geomat. 2014;6:1–15.

19. Al-Najjar HAH, Kalantar B, Pradhan B, Saeidi V, Halin AA, Ueda N, et al. Land cover classification from fused DSM and UAV images using convolutional neural networks. Remote Sens. 2019;11:1461.

20. Yao H, Qin R, Chen X. Unmanned aerial vehicle for remote sensing applications—A review. Remote Sens. 2019;11:1443.

21. Torresan C, Berton A, Carotenuto F, Di Gennaro SF, Gioli B, Matese A, et al. Forestry applications of UAVs in Europe: A review. Int J Remote Sens. 2017;38:2427–47.

22. Crommelinck S, Bennett R, Gerke M, Nex F, Yang MY, Vosselman G. Review of automatic feature extraction from high-resolution optical sensor data for UAV-based cadastral mapping. Remote Sens. 2016;8:689.

23. Timm BC, McGarigal K. Fine-scale remotely-sensed cover mapping of coastal dune and salt marsh ecosystems at Cape Cod National Seashore using random forests. Remote Sens Environ. 2012;127:106–17.

24. Hayes MM, Miller SN, Murphy MA. High-resolution landcover classification using random forest. Remote Sens Lett. 2014;5:112–21.

25. Tamouridou A, Alexandridis T, Pantazi X, Lagopodi A, Kashefi J, Moshou D. Evaluation of UAV imagery for mapping Silybum marianum weed patches. Int J Remote Sens. 2017;38:2246–59.

26. Blaschke T. Object based image analysis for remote sensing. ISPRS J Photogramm Remote Sens. 2010;65:2–16.

27. Kim HO, Yeom JM. Effect of red-edge and texture features for object-based paddy rice crop classification using RapidEye multispectral satellite image data. Int J Remote Sens. 2014;35:7046–68.

28. Torres-Sánchez J, López-Granados F, Peña JM. An automatic object-based method for optimal thresholding in UAV images: Application for vegetation detection in herbaceous crops. Comput Electron Agric. 2015;114:43–52.

29. Blaschke T, Hay GJ, Kelly M, Lang S, Hofmann P, Addink E, et al. Geographic object-based image analysis–towards a new paradigm. ISPRS J Photogramm Remote Sens. 2014;87:180–91.

30. Luca GD, Silva JMN, Cerasoli S, Araújo J, Campos J, Fazio S, et al. Object-based land cover classification of cork oak woodlands using UAV imagery and Orfeo ToolBox. Remote Sens. 2019;11:1238.

31. Ma L, Li M, Ma X, Cheng L, Du P, Liu Y. A review of supervised object-based land-cover image classification. ISPRS J Photogramm Remote Sens. 2017;130:277–93.

32. Ahmed OS, Shemrock A, Chabot D, Dillon C, Williams G, Wasson R, et al. Hierarchical land cover and vegetation classification using multispectral data acquired from an unmanned aerial vehicle. Int J Remote Sens. 2017;38:2037–52.

33. Kilwenge R, Adewopo J, Sun Z, Schut M. UAV-based mapping of banana land area for village-level decision-support in Rwanda. Remote Sens. 2021;13:4985.

© 2026 The Author(s). | Published by Agro Intelligence Research Press

34. Natesan S, Armenakis C, Benari G, Lee R. Use of UAV-borne spectrometer for land cover classification. Drones. 2018;2:16.

35. Lv Z, Shi W, Benediktsson JA, Ning X. Novel object-based filter for improving land-cover classification of aerial imagery with very high spatial resolution. Remote Sens. 2016;8:1023.

36. Geipel J, Link J, Claupein W. Combined spectral and spatial modeling of corn yield based on aerial images and crop surface models acquired with an unmanned aircraft system. Remote Sens. 2014;6:10335–55.

37. Lu DS, Mausel P, Batistella M, Moran E. Comparison of land-cover classification methods in the Brazilian Amazon Basin. Photogramm Eng Remote Sens. 2004;70:723–31.

38. Zhang H, Li J, Wang T, Lin H, Zheng Z, Li Y, et al. A manifold learning approach to urban land cover classification with optical and radar data. Landsc Urban Plan. 2018;172:11–24.

39. Lu D, Weng Q. Use of impervious surface in urban land-use classification. Remote Sens Environ. 2006;102:146–60.

40. USGS. https://www.usgs.gov/landsat-missions/landsat-soil-adjusted-vegetation-index (accessed on 22 December 2021).

41. Immitzer M, Vuolo F, Atzberger C. First experience with Sentinel-2 data for crop and tree species classifications in central Europe. Remote Sens. 2016;8:166.

42. Kindu M, Schneider T, Teketay D, Knoke T. Land use/land cover change analysis using object-based classification approach in Munessa-Shashemene landscape of the Ethiopian Highlands. Remote Sens. 2013;5:2411–35.

43. Dronova I, Gong P, Wang L. Object-based analysis and change detection of major wetland cover types and their classification uncertainty during the low water period at Poyang Lake, China. Remote Sens Environ. 2011;115:3220–36.

44. ESRI. Segmentation in ArcGIS Pro. https://pro.arcgis.com/en/pro-app/latest/help/analysis/image-analyst/segmentation.htm (accessed on 23 February 2022).

45. Zhou W, Troy A. An object-oriented approach for analysing and characterizing urban landscape at the parcel level. Int J Remote Sens. 2008;29:3119–35.

46. Qian Y, Zhou W, Yan J, Li W, Han L. Comparing machine learning classifiers for object-based land cover classification using very high resolution imagery. Remote Sens. 2015;7:153–68.

47. Breiman L. Random forests. Mach Learn. 2001;45:5–32.

48. Cutler DR, Edwards TC, Beard KH, Cutler A, Hess KT, Gibson J, et al. Random forests for classification in ecology. Ecology. 2007;88:2783–92.

49. Haas J, Ban Y. Urban growth and environmental impacts in Jing-Jin-Ji, the Yangtze River Delta and the Pearl River Delta. Int J Appl Earth Obs Geoinf. 2014;30:42–55.

50. Belgiu M, Drăguţ L. Random forest in remote sensing: A review of applications and future directions. ISPRS J Photogramm Remote Sens. 2016;114:24–31.

51. Belgiu M, Drăguţ L. Comparing supervised and unsupervised multiresolution segmentation approaches for extracting buildings from very high resolution imagery. ISPRS J Photogramm Remote Sens. 2014;96:67–75.

52. Congalton RG, Green K. Assessing the Accuracy of Remotely Sensed Data: Principles and Practices. 3rd ed. Boca Raton, FL, USA: CRC Press Taylor and Francis Group; 2019; 48.

© 2026 The Author(s). | Published by Agro Intelligence Research Press

53. Shahtahmassebi A, Yang N, Wang K, Moore N, Shen Z. Review of shadow detection and de-shadowing methods in remote sensing. Chin Geograph Sci. 2013;23:403–20.

54. Milas AS, Arend K, Mayer C, Simonson MA, Machey S. Different colours of shadows: Classification of UAV images. Int J Remote Sens. 2017;38:3084–100.

55. Gage EA, Cooper DJ. Urban forest structure and land cover composition effects on land surface temperature in a semi-arid suburban area. Urban For Urban Green. 2017;28:28–35.

56. Hiscock OH, Back Y, Kleidorfer M, Urich C. A GIS-based land cover classification approach suitable for fine-scale urban water management. Water Resour Manag. 2021;35:1339–52.

57. Hai-yang YU, Gang C, Xiao-san GE, Xiao-ping LU. Object oriented land cover classification using ALS and GeoEye imagery over mining area. Trans Nonferr Metal Soc Chin. 2011;21(Suppl. S3):s733–7.

58. Vanhuysse S, Grippa T, Lennert M, Wolff E, Idrissa M. Contribution of nDSM derived from VHR stereo imagery to urban land-cover mapping in Sub-Saharan Africa. In: Proceedings of the 2017 Joint Urban Remote Sensing Event (JURSE), Dubai, United Arab Emirates; 2017. p. 1–4.

59. Sibaruddin HI, Shafri HZ, Pradhan B, Haron NA. Comparison of pixel-based and object-based image classification techniques in extracting information from UAV imagery data. IOP Conf Ser Earth Environ Sci. 2018;169:012098.

60. Moon HG, Lee SM, Cha JG. Land cover classification using UAV imagery and object-based image analysis—Focusing on the Maseo-myeon, Seocheon-gun, Chungcheongnam-do. J Korean Assoc Geograph Infor Stud. 2017;20:1–14.

61. Mugiraneza T, Nascetti A, Ban Y. WorldView-2 data for hierarchical object-based urban land cover classification in Kigali: Integrating rule-based approach with urban density and greenness indices. Remote Sens. 2019;11:2128.

© 2026 The Author(s). | Published by Agro Intelligence Research Press